The impact of unloading stresses on post-caldera magma intrusions

Published Version:
Gaete A., Kavanagh J.L., Rivalta E., Hilmi Hazim S., Walter T.R., Dennis D.J.C. (2019). The impact of unloading stresses on post-caldera magma intrusions. EARTH AND PLANETARY SCIENCE LETTERS, 508, 109-121 [10.1016/j.epsl.2018.12.016].

Availability:
This version is available at: https://hdl.handle.net/11585/775354 since: 2020-10-21

Published:
DOI: http://doi.org/10.1016/j.epsl.2018.12.016

The impact of unloading stresses on post-caldera magma intrusions

Ayleen Gaete[1], Janine L. Kavanagh[2], Eleonora Rivalta[1], Suraya Hilmi Hazim[2], Thomas R. Walter[1], David J.C. Dennis[3]

[1] GFZ German Research Centre for Geosciences, Telegrafenberg, 14473 Potsdam, Germany

[2] Department of Earth, Ocean and Ecological Sciences, University of Liverpool, Jane Herdman Laboratories, Liverpool L69 3GP, UK.

[3] School of Engineering, University of Liverpool, Liverpool L69 3GH

Corresponding author: Ayleen Gaete (agaete@gfz-potsdam.de)

Abstract

Calderas represent morphological depressions several kilometers in diameter, and the unloaded crustal stresses they produce can form rapidly (e.g. Pinatubo, 1990) or slowly (e.g. Hawaii, 2018). Active calderas are known as sites of persistent magma intrusions, and yet the dynamics of their shallow plumbing system is not well constrained. We use scaled laboratory experiments to study how experimental intrusions are created beneath a caldera by injecting dyed water (magma analogue) into the base of an elastic gelatin solid (crust analogue) with a cylindrical cavity in its surface to mimic a caldera-like topography. The evolving dike geometry and stress field were qualitatively determined using polarized light, and digital image correlation allowed the incremental and total strain to be quantified by tracking passive-tracer particles in the gelatin that fluoresced in a thin 2D vertical laser sheet. Our results show that the unloaded stress field from a caldera can cause a divergence of vertical dikes, and leads to circumferential dikes and cone sheets. When the caldera was large the initially vertical dike became arrested, then grew laterally via circumferentially-propagating en echelon segments; these eventually joined to complete a cone sheet that was parallel to, but extended outside and beneath, the large caldera. When the caldera was small, a circumferential dike erupted, producing a short fissure which was outside, but parallel to, the caldera. We suggest that the distinct curved geometry, velocity, strain and stress characteristics of circumferential dikes and cone sheets can be used to interpret the origin and growth of post-caldera magmatism and the likelihood of eruption in caldera systems.

Keywords: Caldera, cone sheet, gelatin analogue modeling, circumferential dike, digital image correlation

Highlights

- Circumferential dike and cone sheet dynamics are modeled
- Unloaded stress (caldera) affects intrusion geometry, velocity, strain and stress
- Early stages of circumferential dike and cone sheet growth are identical
- Cone sheets grow laterally at depth via en echelon arcuate segments

1. Introduction

Calderas are associated with some of the largest volcanic systems (e.g. Yellowstone, USA) where topographic lows form due to subsidence along caldera ring faults (Cole et al., 2005). Caldera-forming events can be rapid (Mt Pinatubo in Philippines, 1990, e.g. Pallister et al., 1996) or slow (Kilauea volcano in Hawaii, 2018, e.g. USGS, 2018) and may form due to explosive volcanic eruptions (Cole et al., 2005) or gradual drainage of a deep reservoir by lateral intrusion. Despite the largest cataclysmic eruptions being produced during the formation of the caldera itself (Jellinek and DePaolo, 2003), unrest at calderas and relatively small post-caldera eruptions are frequent and pose a significant hazard to the population. Caldera systems are active sites of mineralization, and understanding their development and impact on the volcanic plumbing system is important for georesources, e.g. copper-porphyry deposits (e.g. Blundy et al., 2015), and carbonatite-hosted Rare Earth Elements (e.g. Le Bas, 1987). Irregular topographies and crustal loads are common in volcanic terrains, from tectonic rift zones (e.g. Afar and Iceland) to laterally collapsed sectors of a volcanic edifice (e.g. Mt St Helens, USA), unstable volcanic islands (e.g. La Palma, Canary Islands), ice unloading, and excavation of quasi-cylindrical craters associated with volcanic vents, calderas, tuff cones and diatremes.

Field observations suggest that post-caldera magmatism typically occurs via inclined sheet intrusions (Burchardt et al., 2011). These may take a variety of forms (e.g. Burchardt et al., 2018). In this paper we use the terms 'circumferential dike', which have an arcuate horizontal section, and 'cone sheet', which taper downwards towards a central point and have a circular horizontal section, to distinguish and reflect the end member intrusion geometries, without reference to their process of formation. These intrusion types are common igneous magma bodies, are a major constituent of sub-volcanic plumbing systems, and may feed eruptions in caldera settings (e.g. Bagnardi et al., 2013; Chadwick et al., 2011).

There are several contrasting conceptual models to explain cone sheet formation, but these often do not invoke the presence of a caldera. For example, Galland et al. (2014) carried out an experimental study of cone sheet development by injecting oil into compacted silica flour with a flat topography. They found that cone sheets formed due to a dynamic dimensionless ratio which included the effects of magma viscosity and host-rock deformation mode. In comparison, Magee et al. (2012) proposed that cone sheets form by lateral propagation of regional dikes from an adjacent source, whereas other authors invoke stress changes from a central magma chamber at depth (Anderson, 1936; Geshi, 2005; Johnson et al., 1999; Schirnick et al., 1999). These fundamentally different models demonstrate there remains uncertainty in the growth dynamics of the magmatic system, and cone sheets in particular. Accurately interpreting the surface signals of magma movement for hazard assessment at active volcanoes ultimately depends on the quality of the models upon which these inferences are made (Di Vito et al., 2016; Guldstrand et al., 2017).

The emplacement, propagation and geometry of magma intrusions are influenced by several related factors including density contrasts between magma and host-rock, the ambient stress field (tectonic, regional or local), stress barriers, the physical properties of the intruding magma (e.g. viscosity), and mechanical heterogeneities in the crust such as rock layering and faults (see reviews by Burchardt et al., 2018 and; Rivalta et al., 2015). A commonly explored scenario is that of dike propagation beneath a volcanic edifice where crustal loading influences the tendency for magma to stall at depth or erupt, and whether an eruption occurs in the summit or flank of the volcano (Kervyn et al., 2009; Maccaferri et al., 2011), depending on the magma buoyancy, edifice size and crustal layering (density, rigidity and interface weakness).

The load from a volcanic edifice can cause the attraction of dikes located away from the volcano, and in some cases promote their lateral (blade-like) propagation rather than vertical growth (Watanabe et al., 2002). This supports the hypothesis that dikes change their trajectory during propagation in response to perturbations of the maximum compressive stress (σ_1), whose orientation may vary due to local or regional compression or extension of the medium (Anderson, 1936; Maccaferri et al., 2011; Mathieu et al., 2015; Rivalta et al., 2015).

Magma propagation under a topographic low, such as a caldera, has been relatively unexplored, despite such unloaded stress fields being common features in volcanic terrains (Corbi et al., 2015; Mathieu et al., 2008). Numerical and analogue modeling suggest that a caldera geometry in a volcanic edifice induces unloading stresses that in a cohesive, crystalline rock may favor the emplacement of laminar intrusions with circumferential and/or radial shapes and sills (Corbi et al., 2016, 2015).

Despite the significance of post-caldera magmatism, questions remain regarding the nature of magma intrusion in an unloaded crust. We present results from gelatin laboratory experiments that model the emplacement of a dike in the vicinity of a caldera-like topography. The experiments integrate measurements of sub-surface strain evolution and stress evolution using digital image correlation and polarized light, respectively. Our results test existing models of circumferential dike and cone sheet development and assist in their interpretation by constraining their geometry, propagation pathway, sub-surface deformation and likelihood of eruption.

2. Modeling Framework

2.1. Scaling and selection of analogue materials

Following the approach described by Merle (2015), we define a laboratory prototype scaled geometrically (ratio of distances is constant in nature and the prototype), kinematically (the geometric scaling is maintained over time), and dynamically (the ratio of the mechanical forces between nature and the model is constant). Our selected analogue material for the crust is gelatin, and for magma we have selected water (see Supplementary Table S1 for detailed scaling). Gelatin has been very well studied in scaled laboratory experiments to simulate elastic process in the crust associated with magmatic intrusions (Di Giuseppe et al., 2009; Kavanagh et al., 2013). Gelatin is a visco-elastic material and its transparency allows the evolving dynamic process of dike propagation to be visually tracked in an experiment (Takada, 1990; Watanabe et al., 2002). When used at low concentration (2-5 wt.%) and at low temperature (5-10 °C) it behaves elastically over the timescale of an experiment (Kavanagh et al., 2013), which lasts approximately 10 minutes. Gelatin has been intruded by a range of fluids to simulate dike emplacement (see Janine L Kavanagh et al., 2018 for a review). We have chosen water as the magma analogue as it is a low-viscosity fluid (10^{-3} Pa s) and is slightly less dense than the gelatin ($\Delta\rho$ = 6 kgm^{-3}). It is a suitable analogue to simulate intrusions of low to intermediate viscosity magma that is mostly driven by the overpressure of liquid from a distant source (Kervyn et al., 2009), and it has been used in several previous experiments that study dike propagation (Kavanagh et al., 2018; McLeod and Tait, 1999).

We define the geometric scale between nature n and prototype p in our experiments as the length scale factor:

$$L^* = \frac{L_p}{L_n} \quad [1]$$

Giving L* = 1.0×10^{-5} such that 1 cm in the laboratory represents 1 km in nature, considering that in nature the size of calderas range from 1 km to tens of kilometers in diameter (see Table

S1). An alternative length scale factor is the buoyancy length L_b when magma buoyancy drives the rock fracture (Corbi et al., 2016; Kavanagh et al., 2013; Merle, 2015):

$$L_b^* = \left(\frac{K_c}{\pi^{\frac{1}{2}}\Delta\rho g}\right)^{\frac{2}{3}} \qquad [2]$$

where K_c is the fracture toughness of the host medium, $\Delta\rho$ is the density contrast between host rock and magma, and g is gravity (Taisne and Tait, 2009). Therefore we calculate $L_b^* = 4.1 \times 10^{-5}$ (see Table S1). Overall, the two length scales (Equations 1 and 2) agree as they are within the same order of magnitude.

We have used two contrasting approaches to scale the stresses in our experiments: firstly we scale the elastic deformation of the host material, and secondly we scale the unloading pressure associated with the caldera. Firstly, we calculate the strain scale factor $e*$:

$$e^* = \frac{a}{b} \qquad [3]$$

where a is the dike thickness and b is the dike width. This means $e*$ = 10 when $e_n = 0.002$ and $e_p = 0.02$ in gelatin (Kavanagh et al., 2013). We define a Young's modulus scale factor $E^* = 3 \times 10^{-7}$, as E_n = $10^9 - 10^{10}$ (Kavanagh et al., 2013) and E_p = 300 – 3000 (see Table S1). As the elastic deformation of the gelatin can be defined by the relationship between stress (σ), strain (e) and Young's modulus (E) (Gudmundsson, 2006; Merle, 2015):

$$\sigma^* = E^* e^* \qquad [4]$$

This gives $\sigma^* = 3.0 \times 10^{-6}$ (see Table S1). We also use the unloading pressure scale factor:

$$\sigma^* = P_U^* = \rho_r^* g^* D^* \qquad [5]$$

where D is the caldera depth and ρ_r is the host rock density. As $\rho_r^* = 0.37$ and $D^* = 1 \times 10^{-5}$, this gives $\sigma^* = 3.7 \times 10^{-6}$. The agreement between the stress values calculated from both of these approaches (Equation 4 and 5) confirms that we have properly scaled our experiments.

3. Experimental methodology

3.1. Gelatin Preparation and Young's modulus measurement

We use pigskin gelatin solids (20 Mesh, 260 Bloom; supplied by Gelita UK) prepared at 2.5 wt.% by dissolving the appropriate amount of gelatin powder into water at 80°C. The mixture preparation requires three stages: an initial stage where a concentrated mixture is created and left to cool until it reaches ~ 30°C, then the remaining water is added at 5°C to achieve a mixture temperature of ~23°C. Some experiments required the addition of passive-tracer particles, coated in Rhodamine-B which fluoresces in laser light, to the liquid gelatin in order to apply Digital Image Correlation (DIC) analysis (Sutton et al., 1983). For this purpose, 20-50 µm diameter fluorescent particles (peak fluorescence wavelength: 590 nm) are added to the gelatin mixture following the method described by Kavanagh et al. (2015). A clear-Perspex tank (40 cm square-base, 30 cm high; Figure 1) is then filled up to 23 cm height and the mixture stirred until it reaches the gel point (21°C) to obtain a homogeneous distribution of particles in the solid gel. A caldera-like geometry is established using a round, plastic container (9 or 12 cm diameter) placed onto the gelatin surface and fixed into position relative to the central injection port in the base of the experimental tank using plastic tape. The depth of the caldera is controlled by adding water to the plastic container so that it is submerged by 4 cm depth. Subsequently, the gelatin mixture is covered with vegetable oil which is carefully poured onto its surface to inhibit dehydration, the tank is then covered with plastic wrapping and then left to cool and solidify in a refrigerator set at 5°C for 20 hours. The tank is then taken from the refrigerator, and the plastic container is removed from the center of the gelatin solid by filling it with hot water to allow an easy release and avoid any damage at the floor and/or wall of the caldera that is formed. The oil is then carefully removed using a spoon and paper towel, and the actual depth of the caldera is measured (typically 3-4 cm, see Table 1).

Immediately prior to the experiment starting, the Young's Modulus of the gelatin is calculated by measuring the deflection to the gelatin surface caused by two cylindrical brass loads placed sequentially on the gelatin slab (see Supplementary Table S2 for load properties). The load is placed away from the corner of the tank to minimize any wall effects. The Young's Modulus is calculated using the following equation (Kavanagh et al., 2013):

$$E = \frac{mg(1-v^2)}{\Psi w} \qquad [6]$$

where *m* is the load mass, *g* is the acceleration due to gravity, *v* is the Poisson's ratio (0.5 for gelatin (e.g. Kavanagh et al., 2013; Watanabe et al., 2002)), Ψ is the load diameter, and *w* is the deflection of the surface produced by the load. The average Young's modulus from each load placement is then reported (see Table 1).

3.2. Experiment Setup

Two imaging techniques were used on the experiments to study the subsurface processes associated with dike growth and evolution using two different sets of apparatus: photoelasticity for visualizing stress (Figure 1A), and tracer particle for measuring sub-surface strain and displacement (Figure 1B). To create an experimental dike, a small cut is made in the bottom of the gelatin slab, which controls the orientation of the initial dike. A metal pipe with a tapered end is inserted into this slit and dyed water is injected using a peristaltic pump at a constant volumetric flow rate (*Q*) of 3.9 x 10^{-7} m^3/s. The fluid velocity (V) is approximated by dividing *Q* by the cross-sectional area of the 1 mm-diameter injection outlet. Injections were made at two different offset positions (0.0 cm and 1.0 cm, relative to the center of the caldera) beneath two different caldera sizes (see Table 1).

3.2.1. Photoelasticity setup

Polarized light is known to be a useful tool to visualize the stress distribution in two dimensional elastic problems (Crisp, 1952; Watanabe et al., 2002). We use the photoelastic property of gelatin with the purpose of understanding the interaction of the local stresses with those of the pressurized experimental dike, making a qualitative description of the changes in the stress field during the intrusion development. The sequence of colored fringes represents the gradient of the differential stress ($\sigma_1 - \sigma_3$) perpendicular to the light propagation direction, and the increasing fringe order represents linearly increasing stress (Crisp, 1952); which in the experiments depend on the caldera diameter and caldera depth. The photoelasticity experimental setup (Figure 1A) consists of two polarized sheets attached to the front and back walls of the tank (x-z plane), and two HD video cameras positioned to record images with polarized light (x-z plane, perpendicular to the dike plane) and artificial light (y-z plane, parallel to the dike plane).

3.2.2. Tracer particle setup

The tracer particle experiment setup requires the use of a high intensity laser that was configured to fire at 1 Hz and produce a vertical, thin sheet (approximately 1 mm thick) in the gelatin slab centered on the injection point (Figure 1B, see also Kavanagh et al., 2015). A New Wave Solo-PIV III Nd-YAG Laser provides 50 mJ pulses of energy between 3 and 5 ns and 532 nm wavelength. The laser firing and acquisition is controlled by Dantec Dynamic Studio software and synchronized to a MP CCD camera fitted with a 35 mm Nikon lens (Figure 1B). Longpass (550 nm wavelength) filters fitted to the CCD camera allow only the fluorescent light reflected by the particles to be captured.

A 2D calibration image is required for post-experiment image processing. Prior to the experiment tank being filled with gelatin, the tank is filled with water and a white calibration plate with equally-spaced black dots of known size and spacing was aligned with the laser beam in the center of the experimental tank. An image is then captured for later data pre-processing using DIC.

3.3. Data processing

In order to study the evolution of the growing intrusion geometry, we first track the vertical dike tip trajectory in the x-z plane using video images from the polarized light setup (Figure 1A). This is conducted at intervals of one frame every 5 seconds using the free Java software Tracker vs 4.10.0 (Brown, 2012). The coordinate origin is set as the top of the needle in the calibrated model, and the position of the vertical dike tip is manually tracked over time. The velocity of the dike tip, and the local dip angle relative to horizontal, is simultaneously computed.

DIC is then used to quantify the sub-surface displacement vectors and total strain due to the dike intrusion, at an interval of one image every 5 seconds (0.2 Hz), by using the commercial image analysis tool StrainMaster, implemented in the DaVis software package vs. 8 (LaVision). The calibration image captured prior the experiment is imported into DaVis in a pre-processing stage to scale the results in dimensional units. This process converts the scale from pixels to distance units, and corrects any distortions through the de-warping function. The incremental strain is then calculated by implementing a 'Least Square Matching' algorithm (LSM-algorithm), which operates using an optical flow approach (Fleet and Weiss, 2006). Three seeding points are defined within the reference image, and these are static windows of initial size 121 x 121 pixels that experience no deformation in the experiment. The interrogated area then increases in size with each iteration implementing the 'region grow' algorithm. Outlier and Smoothing filters are then applied, and a mask function is added to exclude the tank walls and caldera cavity from the analysis. The incremental strain is summed to give the total strain.

For very small displacement gradients, the strain tensor values are defined by Cauchy's infinitesimal tensor:

$$\epsilon_{ij} = \frac{1}{2}\left(\frac{\partial v_i}{\partial x_j} + \frac{\partial v_j}{\partial x_i}\right) \quad [7]$$

where *v* is the vector component and *x* the spatial axis. As the experiment observations are carried out in two dimensions (x-z or y-z plane), the lineal deformation in the x or y-direction and in the z-direction are determined by the normal strain components:

$$\epsilon_{xx} = \frac{\partial u}{\partial x} \quad \text{or} \quad \epsilon_{yy} = \frac{\partial v}{\partial y} \quad [8]$$

and,

$$\epsilon_{zz} = \frac{\partial w}{\partial z} \quad [9]$$

Thus, the shear strain is given by:

$$\epsilon_{xz} = \epsilon_{zx} = \frac{1}{2}\left(\frac{\partial u}{\partial z} + \frac{\partial w}{\partial x}\right) \quad \text{or} \quad \epsilon_{yz} = \epsilon_{zy} = \frac{1}{2}\left(\frac{\partial v}{\partial z} + \frac{\partial w}{\partial y}\right) \quad [10]$$

4. Results

In total 19 experiments were conducted to explore the influence of caldera unloading and injection offset on dike propagation, geometry and growth. The experimental results are grouped into two end-member geometries: circumferential dikes and cone sheets, however transition geometries are also observed (see Table 1). We detail our experimental observations and results below using representative experiments as examples grouped by their end-member geometries.

4.1. Circumferential dikes

Circumferential dikes are formed in our experimental series only in the presence of a small caldera (Table 1) and in three stages: 1) sub-vertical dike, 2) inclined sheet, and 3) ascent to eruption (see Supplementary Video Figure S1). When the injection position is offset, these three stages occur earlier and their transitions happen at greater depth than when the injection is central. The details of each stage of circumferential dike formation and eruption are now described.

4.1.1. Stage I: Sub-vertical dike

Polarized light shows the unloading stress field induced by the caldera in the pre-injection state (Figure 2Ai). When the injection starts, a vertical dike is produced (Figure 2Aii and 2Bii) creating its own stress field that is focused in a small region around the dike tip and intensifying in magnitude and extent as the dike grows upwards until it reaches a vertical length of 9.2 cm by the end of this stage (Figure 2Aii). At this time, the dike grows near vertical with a dip angle of approximately 80° (Figure 3A). During this stage there is an initial rapid acceleration followed by velocity deceleration (Figure 3B). The DIC analysis (Figure 4) shows the displacement vectors are small and radiate out from the entire dike length, and the total normal strain component e_{xx} (Figure 4Bi) is large (14×10^{-2}) compared with the vertical (e_{zz} 4×10^{-2}, Figure 4Ci) and shear components (e_{xz} 4.5×10^{-2}, Figure 4Di).

4.1.2. Stage II: Inclined sheet

In Stage II, the dike moves away from the caldera center with a maximum height of 12.8 cm in the end of this stage (Figure 2Aiii and 2Biii). In terms of stress, this stage is distinguished by the colored fringes from the dike visually interacting with those of the caldera (Figure 2Aiii). It coincides with a rapid decrease in the dip angle (from 80° to 40°, Figure 3A) and a slight acceleration of the vertical tip (Figure 3B). Overall the direction of displacement is upwards and towards the caldera, and its maximum amplitude is less than 5 mm (Figure 4Aii, Bii, Cii). The total strain during Stage II (Figure 4Aii) has slightly decreased in the normal horizontal strain (e_{xx} down to 11×10^{-2}), but has increased in the vertical and shear components (e_{zz} and e_{xz} up to 10×10^{-2} and 9×10^{-2}, respectively); e_{xx} is distributed along the length of the vertical dike and inclined limb (Figure 4Bii), whereas there are local concentrations in e_{zz} (Figure 4Cii) and e_{xz} (Figure 4Dii) at the tip.

4.1.3. Stage III: Ascent to eruption

The final stage of circumferential dike development is acceleration to eruption to form a circumferential fissure (Figure 2Aiv and 2Biv). In our experiments all circumferential dikes erupted. During this final stage, there is no visual interaction between the dike stress field and that from the caldera. The dike dip angle gradually increases to 60° and then broadly maintains this (Figure 3A). The vertical tip decelerates gradually, but then accelerates towards eruption (Figure 3B). The maximum opening of the inclined limb of the dike is 7.8 mm thick (Figure 4 Aiii), generating the largest magnitude of the total displacement vectors which are oriented towards the caldera (Figure 4Biii, Ciii, Diii). The total strain just before eruption produces the maximum deformation during injection, producing visible uplift of the caldera floor. The largest component of total strain is vertical at e_{zz} 22.5×10^{-2} (Figure 4Ciii), with similar values in total horizontal and shear strain (e_{xx} and e_{xz} up to 17.5×10^{-2}; Figure 4Biii and 4Diii).

4.2. Cone sheets

Cone sheets were formed in the presence of the large caldera six times (see Table 1), and transitional geometries (partial cone, but with dike eruption) were formed four times. The cone sheets are formed in four stages (see Supplementary Video Figure S2), with the first two stages being identical to the circumferential dike formation. Stage I is a sub-vertical dike, Stage II is an inclined sheet, Stage III is lateral growth, and Stage IV is cone sheet completion. Similarly to the circumferential dike, when the injection position is offset this results in earlier and deeper transitions between the stages.

4.2.1. Stage I: Sub-vertical dike, and Stage II: Inclined sheet

The pre-injection stress pattern induced by the large caldera shows more fringes that extend to greater depths in the gelatin slab (Figure 5Ai) compared to the small caldera (Figure 2Ai). Similarly to the small caldera experiments, the first two stages of cone sheet growth are: 1) sub-vertical dike (Figure 5Aii, Bii), which then changes dip and develops into 2) an inclined sheet (Figure 5Aiii, Biii). During Stage I we observe a moderate decrease in the dip angle from 85° to 75° (Figure 3C) and velocity deceleration (Figure 3D), as the dike reaches 9.3 cm height. During Stage II the dike changes dip angle from 75° to 35°, accelerates from 0.6 to 1.4 cm/s, and reaches 12.6 cm height by the end of Stage II.

The total displacement and total strain (normal and shear components) of cone sheet growth are measured in the x-z plane (Figure 6) and y-z plane (Figure 7). During Stages I and II, the majority of the propagation is out of the y-z plane and so only minor displacements and total strain are recorded in this view (Figure 7Ai, Bi, Ci, Di, Aii, Bii,Cii, Dii). Stage I of cone sheet formation (Figure 6Ai) has maximum total strain in the horizontal normal component ($e_{xx} = 11 \times 10^{-2}$, Figure 6Bi), with this distributed across the whole dike, with lower vertical and shear total strain components (e_{zz} and $e_{xz} = 4 \times 10^{-2}$; Figure 6Ci and 6Di). In contrast, Stage II has maximum total strain in the vertical normal component ($e_{zz} = 12 \times 10^{-2}$; Figure 6Cii), with lower horizontal and shear total strain components (e_{xx} and $e_{xz} = 8 \times 10^{-2}$; Figure 6Bii and 6Dii). There are also similar displacement vectors to those observed in Stages I and II of the circumferential dike formation, with low magnitude displacements (<5 mm in Stage I, and 5-10 mm in Stage II) radiating out from the dike.

4.2.2. Stage III: Lateral dike growth by arcuate segments

Following initial vertical dike growth (Stage I) and then divergence to a dipping dike (Stage II), a new direction of intrusions establishes at the turning point *h* (see Table 1). Stage III of cone sheet growth is marked by the Stage II dike dip angle stabilizing at approximately 60° (Figure

3C), and the vertical growth rapidly decelerating indicating an arrested dike (Figure 3D). Two circumferential and laterally-propagating en echelon arcuate segments then form close to the turning point (Figure 3C), specifically from the lower part of the inclined sheet (Figure 5Aiv and 5Biv). In the x-z plane, the total displacement vectors increase in magnitude relative to Stage II to be >10 mm, and the maximum displacement continues being oriented radially towards the caldera (Figure 6Biii, Ciii, Diii). The largest total strain is the vertical normal component ($e_{zz} = 37.5 \times 10^{-2}$; Figure 6Ciii) followed by the shear component ($e_{xz} = 23 \times 10^{-2}$; Figure 6Diii) and horizontal normal component ($e_{xx} = 20 \times 10^{-2}$; Figure 6Biii). In Stage III, the cone sheet emerges in the y-z plane as the inclined, laterally-propagating arcuate segments penetrate the laser sheet (Figure 7Aiii). This produces maximum total displacement of 10 mm (which is slightly less than measured in the x-z plane), and a maximum vertical deformation ($e_{zz} = 12 \times 10^{-2}$; Figure 7Ciii) compared to horizontal ($e_{yy} = 7 \times 10^{-2}$; Figure 7Biii) and shear components ($e_{yz} = 9 \times 10^{-2}$; Figure 7Diii); which are all lower than strains measured in the x-z plane.

4.2.3. Stage IV: Cone sheet completion

The fourth and final stage of cone sheet formation is the completion of the cone geometry (Figure 5Av and 5Bv). This occurs when the laterally-propagating arcuate segments of Stage III join to create a circular profile in the horizontal plane without erupting. The final cone sheet geometry has a range of forms spanning 'cocktail-glass', 'bowl' and 'trumpet' forms (Figures 5, 6 and 7), in agreement with cone sheet geometries described by Burchardt et al. (2018). In transitional geometries, Stage III still produces the lateral sub-surface arcuate segments but they do not join. Instead, at some moment the vertical ascent of the dike is reinitiated, at the location where it first became arrested, and this results in an eruption. Therefore, transitional geometries do not reach Stage IV and have growth behavior and a final geometry that is intermediate to the circumferential dike and cone sheet**.**

Stage IV has a slight decrease in the dip angle starting immediately after the arcuate segments join (Figure 3C), and the velocity decrease is maintained (Figure 3D). The thickest opening of the inclined sheet was 13.63 mm (Figure 6Aiv), which produced displacements greater than 10 mm focused directly beneath and towards the caldera (Figure 6Biv, Civ, Div). The maximum strain occurs in the vertical normal component, reaching $e_{zz} = 55 \times 10^{-2}$ in the x-z plane (Figure 6Civ) and $e_{zz} = 50 \times 10^{-2}$ the y-z plane (Figure 7Civ). The total strain is up to $e_{xx} = 20 \times 10^{-2}$ and $e_{yy} = 12 \times 10^{-2}$ in the horizontal components (Figures 6Biv and 7Biv, respectively), and $e_{xz} = 35 \times 10^{-2}$ and $e_{yz} = 22.5 \times 10^{-2}$ in the shear component (Figures 6Div and 7Div, respectively).

5. Discussion

5.1. Circumferential dike or cone sheet? Comparison with previous experiments

Our experimental series has produced a spectrum of thin sheet-like intrusions, all of which were parallel to the circular caldera, and with end-member geometries of an erupted circumferential dike (Figure 2) and an intrusive cone sheet (Figure 5). The development of these different end-member geometries was similar. Both circumferential dikes and cone sheets propagated at dip angles which reached almost vertical (Figure 3A, C; Figure 8), but the circumferential dikes dip angle ranged from ~40° compared to 30° for the cone sheets (Figure 8). These dip values are similar to those in nature, for example the trachytic to phonolitic cone sheets of the Tejeda Complex, Gran Canaria which intruded intra-caldera deposits (Schirnick et al., 1999), and the mafic cone sheets of the Ardnamurchan central igneous complex, NW Scotland which intruded into the base of an ancient basaltic volcano (Richey and Thomas, 1930).

Circumferential dikes and cone sheet geometries have been studied in previous laboratory experiments. Using a granular material to represent the properties of the brittle crust and a flat topography, Galland et al. (2014) found that cone sheets form when the magma source is shallow with respect to the intrusion's width, or when the injection velocity or viscosity is high. Corbi et al. (2016) created buoyant air-filled dikes in gelatin edifices which had a topographic depression simulating a caldera. Similarly to our experiments, they observed that the unloading stress field leads to the formation of circumferential dikes. They found that magma buoyancy plays a key role in the dike geometry and the eruption location, and our experiments support this work even though we did not include a volcanic edifice. When the unloading stresses were particularly large we found this was able to stop eruption and cause a full-cone sheet to develop, whereas Corbi et al. (2016) did not form cone sheets.

The caldera diameter was the key parameter in determining the outcome of our experiments: circumferential dikes always developed in the presence of the 9 cm caldera diameter, and a spectrum of transitional to cone sheet geometries were associated with the 12 cm caldera diameter topography (see Table 1). Following the approach of Galland et al. (2014), we have analyzed our experiments further by considering the outcomes related to dimensionless Pi-numbers (Figure 9). The first Pi-number is geometric:

$$\Pi_1 = \frac{h}{d} \qquad [11]$$

where *h* is the depth at which bending of the dike first occurs, and *d* is the horizontal extent of the intrusion (see Table 1). The second Pi-number considers the fluid-flow properties and extent of unloading stress relative to lithostatic loading:

$$\Pi_2 = \frac{\mu v}{d(P_L - P_U)} \qquad [12]$$

where μ is the fluid viscosity, V is the velocity of the fluid, P_L is the lithostatic pressure, and P_U is the unloading pressure due to the presence of the caldera (see Supplementary Table S1). Figure 9 shows our experiments occupy three distinct regions in this non-dimensional space, with cone sheets forming at low Π_1 and Π_2 values, circumferential dikes forming at high Π_1 and Π_2 values, and transitional geometries forming at intermediate Π_1 and Π_2 values. Geophysical constraints on parameter values that would populate the Π_1 and Π_2 equations in nature (see Supplementary Table S1 for example) suggest that magnitudes of Π_1 and Π_2 in nature are high compared to our experiments. For example, at Rabaul Volcano in Papau New Guinea (Kennedy et al., 2018) the corresponding Π_1 value is 1.5 and the Π_2 value is 3×10^{-5}. This means, according to our models, the most likely intrusion form geometry at Rabaul Volcano would be circumferential dikes.

5.2. Circumferential dikes and cone sheets in nature

The Ardnamurchan cone sheets are perhaps the most-famous of all cone sheets, but there are contrasting models to explain their origin. Burchardt et al. (2013) used 3D projections to propose that the Ardnamurchan cone sheets originate from a single, elongated and temporally evolving magma chamber. This model is in contrast to Richey and Thomas (1930) who originally proposed three centers, and Magee et al. (2012) who proposed lateral magma flow from an adjacent magmatic source in a compressional stress field. We show experimentally that local unloading stresses can cause an initially vertical dike originating from directly beneath a caldera to stall in the crust and grow laterally to form a cone sheet. This is relevant to the Ardnamurchan central igneous complex, as our model does not require input from neighboring systems to build a cone sheet (in contrast to Magee et al., 2012) and does not make assumptions about the nature of the magma chamber at depth (as is the case in Burchardt et al., 2013). Instead we demonstrate that such geometries could be formed purely due to local unloading stresses. It is unclear whether or not there was a caldera present at the time when the Ardnamurchan cone sheets formed (Brown and Bell, 2006), but calderas are thought to have been present in the region at the time of intrusion (Troll et al., 2000).

Articulated magma intrusion geometries, made up of circumferential sub-vertical dikes close to the caldera rim which dip towards sub-horizontal sills below the caldera floor, have often been needed to fit crustal deformation data at calderas. Geodetic studies of magma intrusion associated with the 2005 circumferential fissure eruption of Fernandina volcano in the Galapagos (summit caldera: 5 km x 6.5 km) presented pre-eruptive (Bagnardi et al., 2013) and co-eruptive (Chadwick et al., 2011) surface deformation that was recorded using Interferometric synthetic aperture radar (InSAR). Inverse models of the data suggested the intrusion which fed the eruption had a curved and circumferential laminar geometry and originated from a sill, thus showing similar geometry to our experimental circumferential dikes. The continuous vertical growth and final eruption of our experimental circumferential dike agrees well with the Chadwick et al. (2011) model of intrusion leading to the 2005 eruption of Fernandina (Corbi et al., 2015).

Overall, we suggest that the common modeling assumption of flat geometries, such as planar sheets opening dislocations or cracks, the availability of suitable analytical solutions, and the need to keep the number of model parameters low, may have limited our ability to recognize curved geometries such as those we propose here. Deep cone sheet intrusions may produce low-amplitude uplift that may be a satisfyingly fit for pressurized sub-horizontal cracks below the caldera floor, which is a feature ubiquitously found by geophysical and geodetic surveys at calderas worldwide.

5.3. Arcuate segment development and lateral dike growth

Lateral propagation of a circumferential dike has been evidenced by geological records, but rarely from geophysical monitoring. Geological evidence of lateral flow during cone sheet development was found by Magee et al. (2012) using magnetic fabrics preserved within crystalline cone sheets. However, they interpreted this as evidence of magma being sourced from an adjacent magma chamber, but our results show that such crystalline fabrics could result from a cone sheet intrusion whose magma source was directly beneath an unloaded topography. Geophysical evidence of lateral propagation of a circumferential dike firstly came from the 1989 seismic swarm at Mammoth Mountain, Long Valley caldera, California (Prejean et al., 2003) where earthquake hypocenter migration into a ring structure was interpreted as fluid which triggered seismicity on a ring fault, but it would be also consistent with lateral propagation (0.4 km/month) of a conical opening crack filled with magma or other magmatic fluid evidenced by the migration of seismicity over time. Therefore, our model observations are support the interpretation of lateral magma migration recorded by the seismic data. Secondly, reconstructing ground displacement at the pre-eruptive phase in Monte Nuovo, Campi Flegrei caldera (1935 AD), Di Vito et al. (2016) recognized a circumferential source extending from the center, eccentrically towards the caldera rim, that transfers felsic magma laterally to feed eruptions at the caldera margin, which has been the eruptive magma path for the last 5 ka. In the laboratory, both circumferential dikes and cone sheets had their lowest ascent velocities when the dikes were growing at intermediate dip angle (40-80°), and their highest velocities coincided with the lowest and highest dip angles (Figure 8).

Circumferential lateral propagation was present in the growth of our experimental cone sheet intrusions by the establishment of laterally propagating arcuate segments, and the cone sheet geometry initiated at the bending location of the dike (h). We interpret the development of en echelon arcuate segments in our experiments to be associated with stress rotation, due to the influence of the caldera stress field which causes lateral propagation and crack opening under mixed-mode loading (Mode I and Mode III) thus creating shear at the growing tip (Pollard et al., 1982).

5.4. Limitations of our models

Our experimental approach was not to reproduce the natural complexity of magma intrusion in the presence of calderas, but to focus on the effect of the magnitude and extent of the unloading stress on the type of intrusion formed and how it grew. Inelastic host-rock deformation was not considered in our models, and yet this may be important in the shallow crust and in a caldera setting in particular, where rocks may have been damaged due to the caldera-forming process (see Galland et al., 2018 for a review). On a local scale, an inelastic host-rock rheology may dampen the transference of rock deformation signals, due to local compaction and grain rotation, and may increase the possibility of dike segmentation occurring. We did not consider rock layering, yet volcanic settings are likely to be mechanically variable, and previous work has demonstrated how rigidity layering can promote the formation of sills beneath a rigid layer (Kavanagh et al., 2006). Calderas also have fault systems that are likely to influence magma propagation (Browning and Gudmundsson, 2015). Recent experimental work using particle image velocimetry (Kavanagh et al., 2018; Kavanagh, 2018) to model magma flow in dikes is challenging existing dike propagation models, and demonstrates how consideration of the host rock deformation and the magma flow dynamics are needed to develop the next generation of dike emplacement models. The additional impacts of faults, mechanical layering and magma flow dynamics on magma propagation in caldera settings should be the focus of future multidisciplinary and experimental work.

6. Conclusions

We produced experimental circumferential dikes which erupted, and intrusive cone sheets that grew by lateral propagation of en echelon arcuate dike segments. Both originated from a single dike beneath a caldera-like topography in an elastic material. We also formed transitional geometries that were intermediate to these end-member forms. Circumferential dike and cone sheet intrusion dynamics occurred in stages of development which are reflected by their geometric (dip angle), kinematic (velocity) and dynamic (stress and strain) evolution. We identified 3 stages of circumferential dike development (I. Sub-vertical dike; II. Inclined sheet; III. Ascent to erupt) and 4 stages of cone sheets (I. Sub-vertical dike; II. Inclined sheet; III. Lateral growth by arcuate en echelon dike segments, and IV. Completion of the cone sheet). Our results show there are many similarities between the dynamics of cone sheets and circumferential dikes. Our summative dimensionless phase diagram suggests that their occurrence can be related to geometric, fluid flow, and lithospheric unloading conditions.

We have proposed a new origin and emplacement for cone sheets that originate from purely vertical dike growth. However, our analysis suggests that conditions in nature seem to be unfavorable for cone sheets to form due to crustal unloading in a caldera setting, and that circumferential dikes and transitional-cone sheet geometries are more likely to form. Our models can help the interpretation of InSAR, GPS and seismic data from active systems, and contribute to the production of more accurate models of magma sources beneath calderas. An important new implication of our models for volcano monitoring is that the conditions for circumferential dike formation appear to be more prevalent in nature. Significantly, it may not be possible to distinguish whether an intrusion will be likely to erupt or not until it has propagated into the shallow crust, which is when it is also likely to be propagating at its fastest rate. This new understanding of magma intrusion dynamics will help to reconstruct the history of ancient calderas, and to forecast unrest and eruptions in active ones.

Acknowledgments

This research was supported by the German Research Centre for Geosciences, GFZ and the ERC Volcapse project, and by the program Forschungsstipendium für Doktorat from Deutscher Akademischer Austausch Dienst DAAD awarded to AG. AG and SHH wish particular thanks to members of the Liverpool MAGMA Laboratory Elliot Wood and Simon Martin for their assistance in the development of this work. SHH acknowledges support from the Malaysian Government and the National University of Malaysia. AG especially thanks to Mehdi Nikkhoo for long discussions and advice related to this work and other topics and for help with conducting earlier models. We thank Steffi Burchardt and Craig Magee for thoughtful reviews which improved the manuscript, and we thank Tamsin Mather for editorial support.

Tables and Figures

Experiment code	C [cm]	X [cm]	D [cm]	Wt.%	H [cm]	t [hr]	T [°C]	E [Pa]	Q [m^3/s]	Result	h [cm]	d [cm]	Analysis Method
AG-07	9.0	0.0	3.31	2.5	22.6	20.5	5	2675	3.9×10^{-7}	C. dike	8.2	13.0	PL, TT
AG-13	9.0	0.0	3.78	2.5	23.1	20.5	5	2843	3.9×10^{-7}	C. dike	10.7	13.3	TP
AG-09	9.0	1.0	3.04	2.5	23.2	21.0	5	2490	3.9×10^{-7}	C. dike	8.8	13.8	PL, TT
AG-08	12.0	0.0	3.94	2.5	23.5	20.0	5	3113	3.9×10^{-7}	Cone sheet	12.1	22.4	PL, TT
AG-06	12.0	0.0	3.52	2.5	22.4	19.8	5	2779	3.9×10^{-7}	Cone-Trans	10.7	17.5	-
AG-14	12.0	0.0	4.20	2.5	23.5	21.0	5	2739	3.9×10^{-7}	Cone-Trans	11.1	16.9	-
AG-15	12.0	0.0	3.65	2.5	23.5	21.1	5	2586	3.9×10^{-7}	Cone-Trans	9.8	17.7	-
AG-16	12.0	0.0	3.77	2.5	23.2	20.5	5	2902	3.9×10^{-7}	Cone-Trans	16.8	17.5	-
AG-10	12.0	1.0	3.55	2.5	22.5	21.0	5	2401	3.9×10^{-7}	Cone sheet	12.0	23.4	PL, TT
AG-05	12.0	1.0	3.58	2.5	23.1	19.7	5	2721	3.9×10^{-7}	Cone sheet	14.3	23.7	TT
AG-17	12.0	1.0	3.95	2.5	23.2	19.7	5	2580	3.9×10^{-7}	Cone sheet	15.2	24.5	TP
AG-19	12.0	1.0	3.80	2.5	23.1	19.0	5	2964	3.9×10^{-7}	Cone sheet	15.3	24.0	TP
AG-18	12.0	2.0	3.90	2.5	23.2	22.0	5	3031	3.9×10^{-7}	Cone sheet	14.5	23.9	TP

Table 1: Model parameters, observed results, and methods applied in the experiment analysis. The experiments are listed in order of caldera diameter C and offset injection position X. The measured caldera depth D, gelatin concentration Wt.%, thickness of gelatin slab H, time left to cure t, refrigerator temperature T, average Young's modulus E, and injection flux of fluid Q is reported. 'Result' corresponds to the final geometry of the intrusion classified as 'C. dike' (circumferential dike), 'Cone sheet', or 'Cone-Trans' for transitional geometries, and the final depth of bending h, and extent of intrusion d are also reported. The analysis methods used are: Polarized light (PL), vertical tip tracking (TT) and tracer particles (TP).

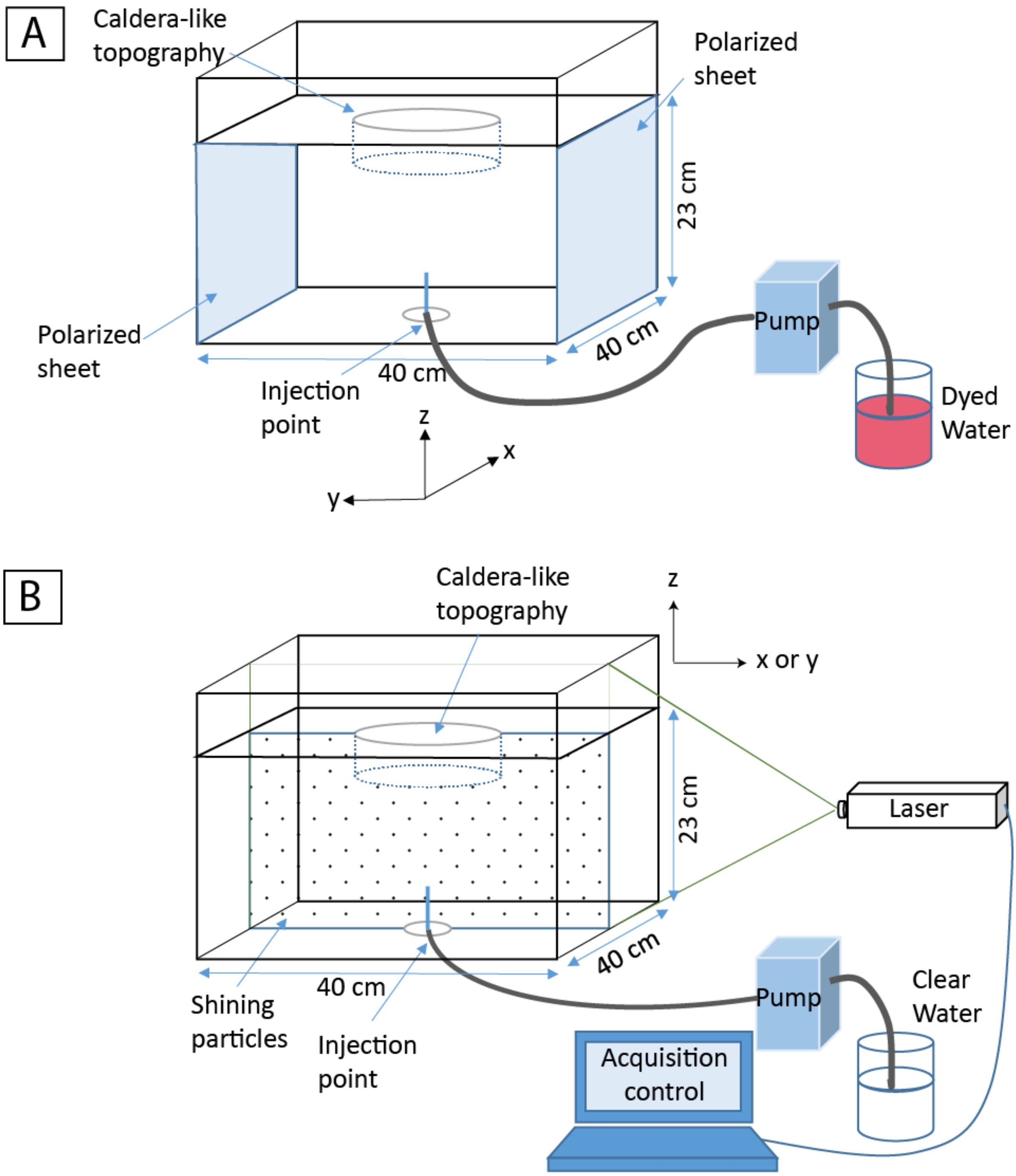

Figure 1: Schematic diagram of the experimental setups. A) Polarized light experiment: dyed water is injected into the base of a gelatin slab using a peristaltic pump. The gelatin surface is modeled to have a caldera-like topography, and stress in the gelatin is visualized using two parallel polarized sheets attached to the tank walls on the x-z plane and perpendicular to the initial dike profile. Two HD video cameras (not shown) record images the x-z and y-z directions. B) Tracer particle experiment: a high intensity vertical laser sheet illuminates a 2D profile (either x-z plane or y-z plane) through the center of the tank and exciting passive-tracer fluorescent particles in the gelatin. A CCD camera records the illuminated plane at 1 frame per second, synchronized with the laser.

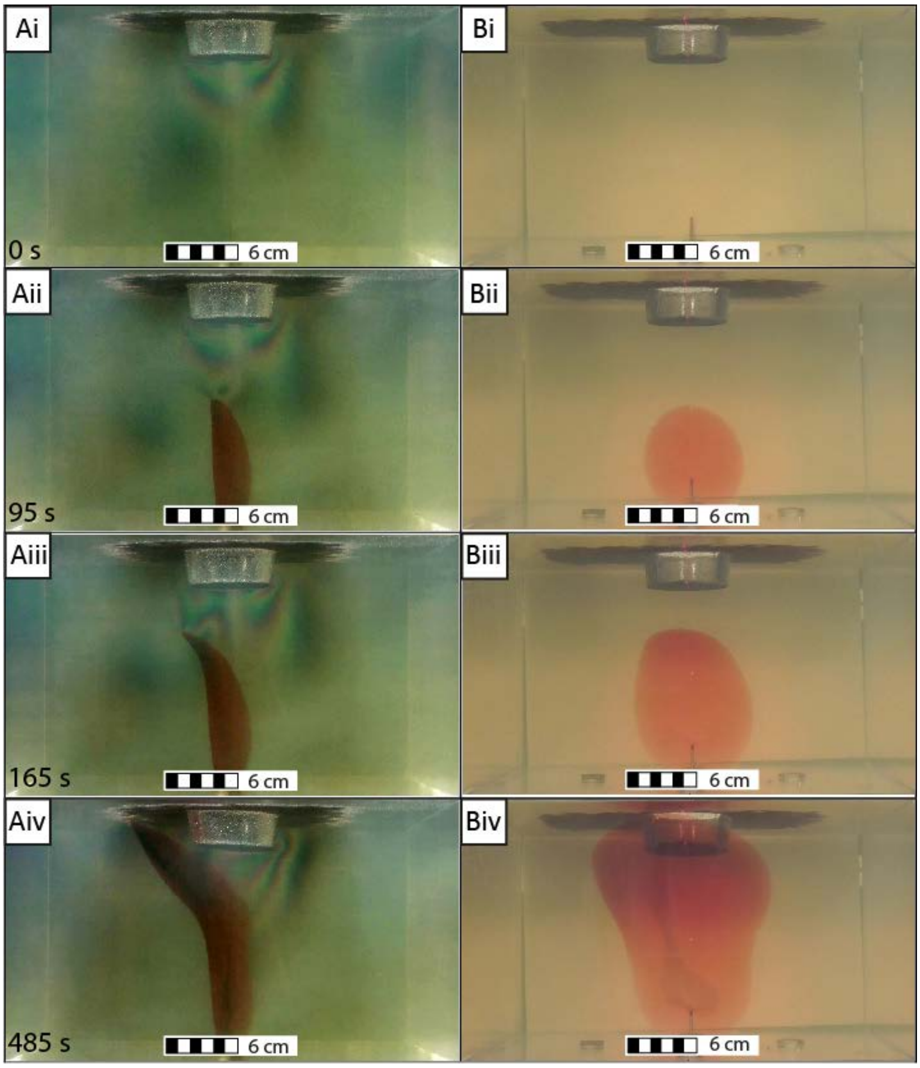

Figure 2: Photographs of circumferential dike development in the presence of a small caldera (Experiment AG-07, see Table 1): A) Polarized light (x-z plane), and B) artificial light (y-z plane). i) Pre-injection state, ii) Stage I: sub-vertical dike (95 s), iii) Stage II: inclined sheet (165 s), iv) Stage III: ascent to eruption (485 s). See also Supplementary Video Figure S1.

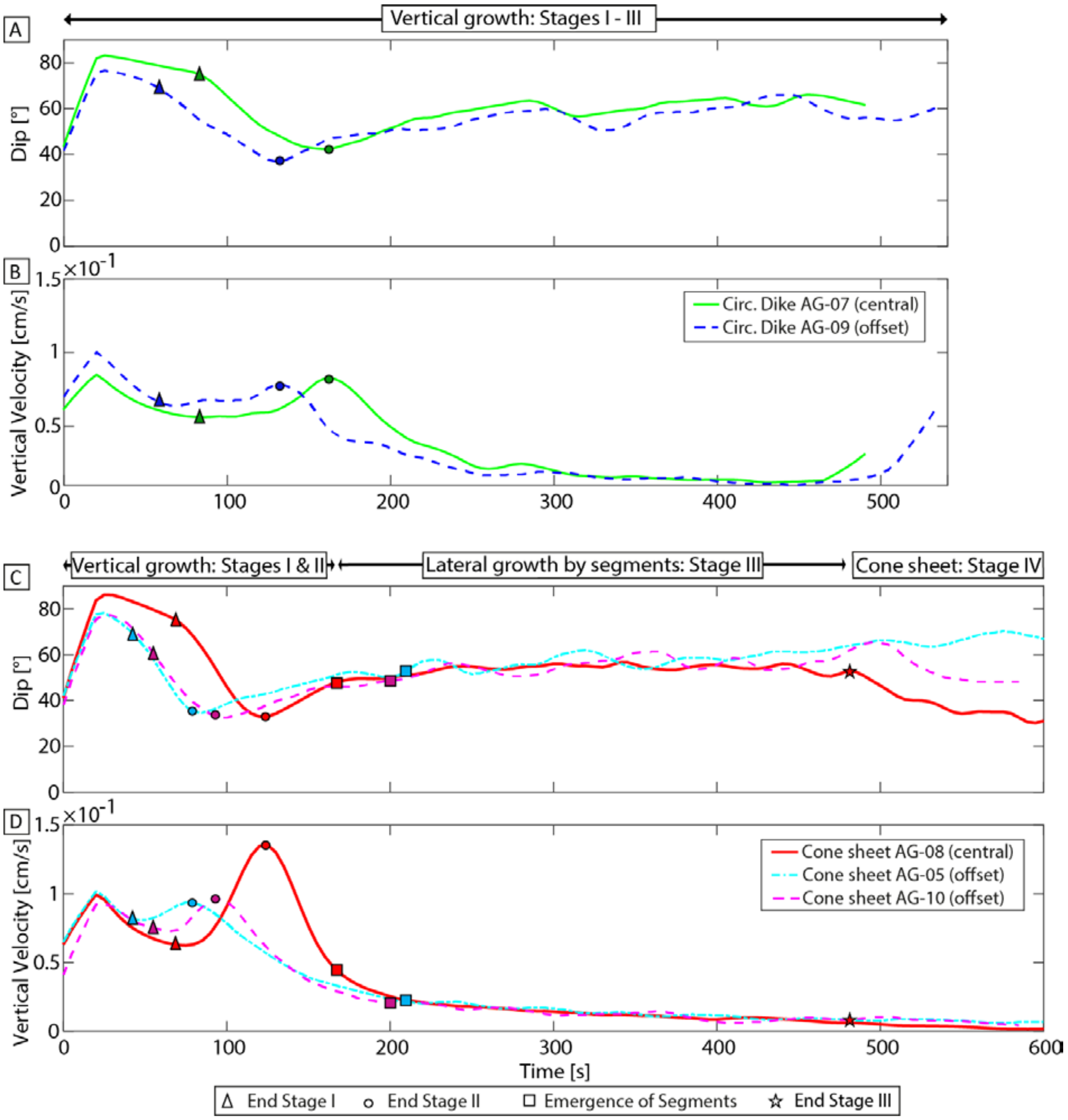

Figure 3: Three stages of circumferential dike (A-B) and four stages of cone sheet (C-D) growth shown by changes in Dip angle (°) and velocity (cm/s) of the vertical dike tip in the presence of the caldera. The approximate timings of stage transitions is indicated at the top of the graphs (A for circumferential dikes, and C for cone sheets). In the graphs the triangle indicates the end of Stage I (sub-vertical dike), the circle indicates the end of Stage II (inclined sheet), and the star indicates the end of Stage III (lateral growth by arcuate segments in cone sheet emplacement). Stage III shows the ascent to eruption in circumferential dike emplacement. The Stage III of cone sheet growth produces laterally propagating arcuate segments (the time of their emergence is indicated by a square) and these join at the start of Stage IV to complete the geometry.

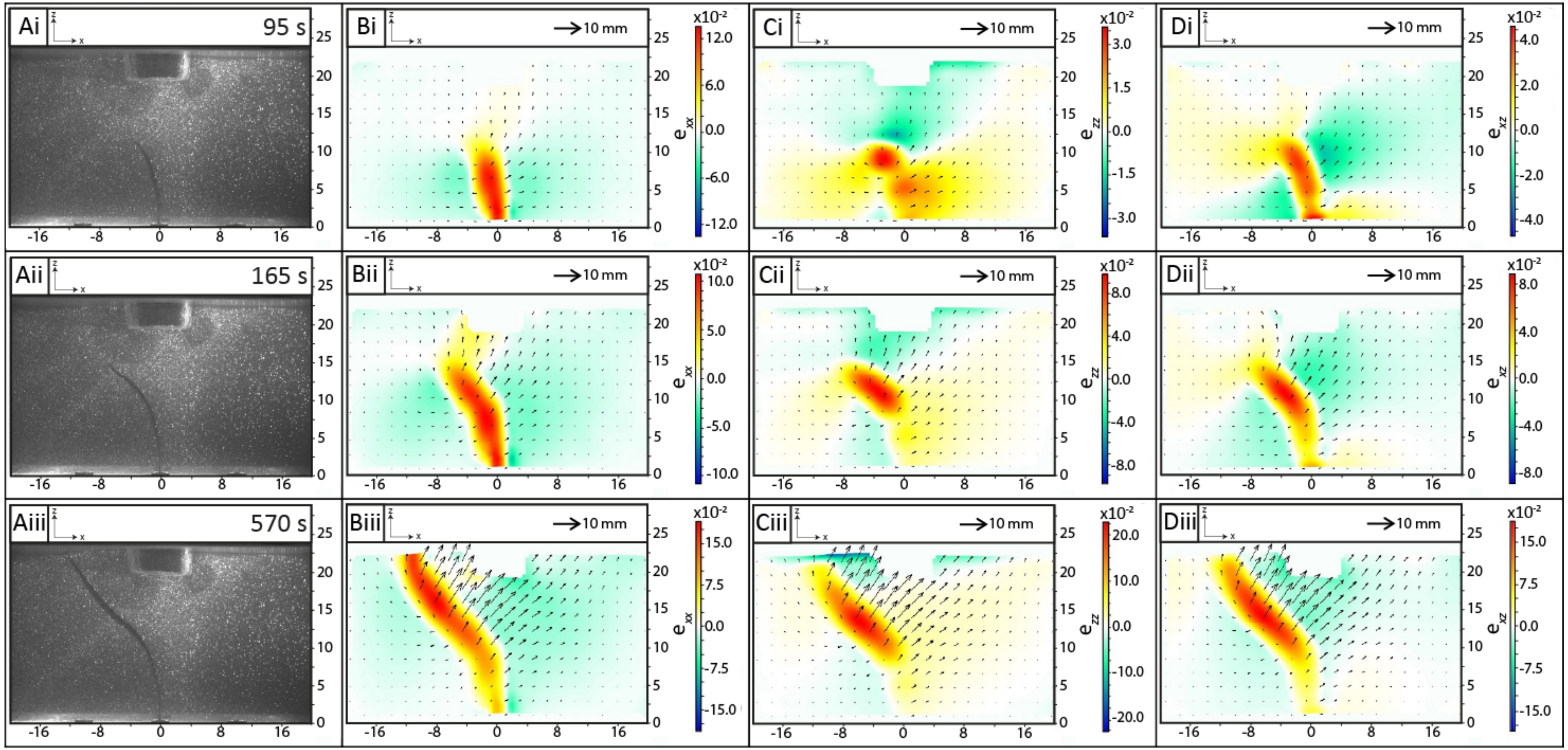

Figure 4: Three stages of circumferential dike development in the presence of a small caldera, imaged in the x-z plane, with sub-surface total strain (color maps) and displacement (vector arrows) calculated using DIC (Experiment AG-13, see Table 1): i) Stage I: initial sub-vertical dike (95 s), ii) Stage II: inclined sheet (165 s), and iii) Stage III: ascent to eruption (570 s). A) Dewarped experimental images, B) horizontal total normal strain e_{xx}, C) vertical total normal strain e_{zz}, and D) total shear strain component e_{xz} are shown. The red color represents extensional deformation in the normal components and anticlockwise rotational deformation in the shear component. See also Supplementary Video Figure S1.

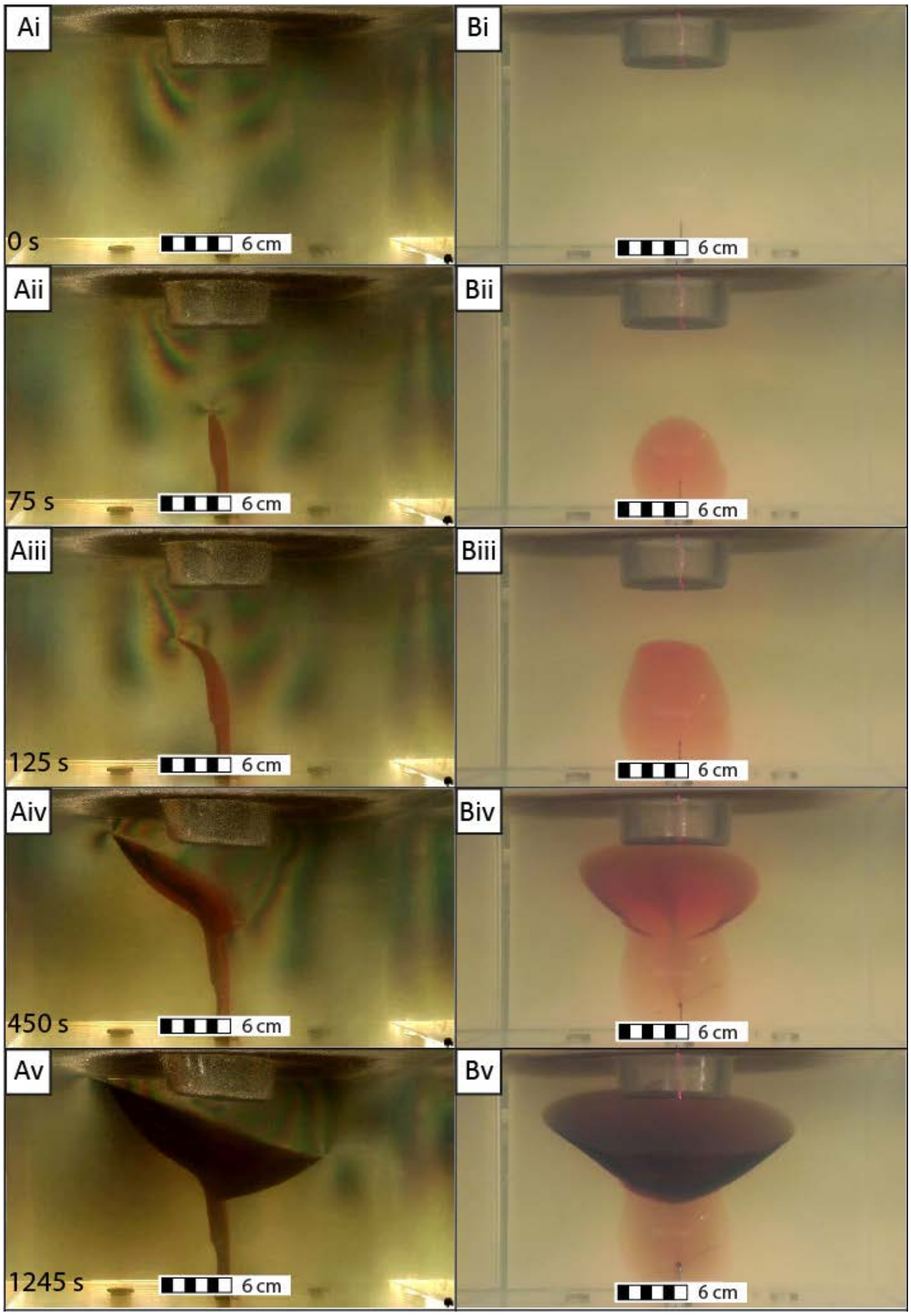

Figure 5: Photographs of cone sheet development in the presence of a large caldera (Experiment AG-08, see Table 1): A) Polarized light (x-z plane), B) artificial light (y-z plane). i) Pre-injection stress state, ii) Stage I: sub-vertical dike (75 s), iii) Stage II: inclined sheet (125 s), iv) Stage III: lateral growth by en echelon arcuate segments (450 s), and v) Stage IV: cone sheet completion with no eruption (1245 s). See also Supplementary Video Figure S2.

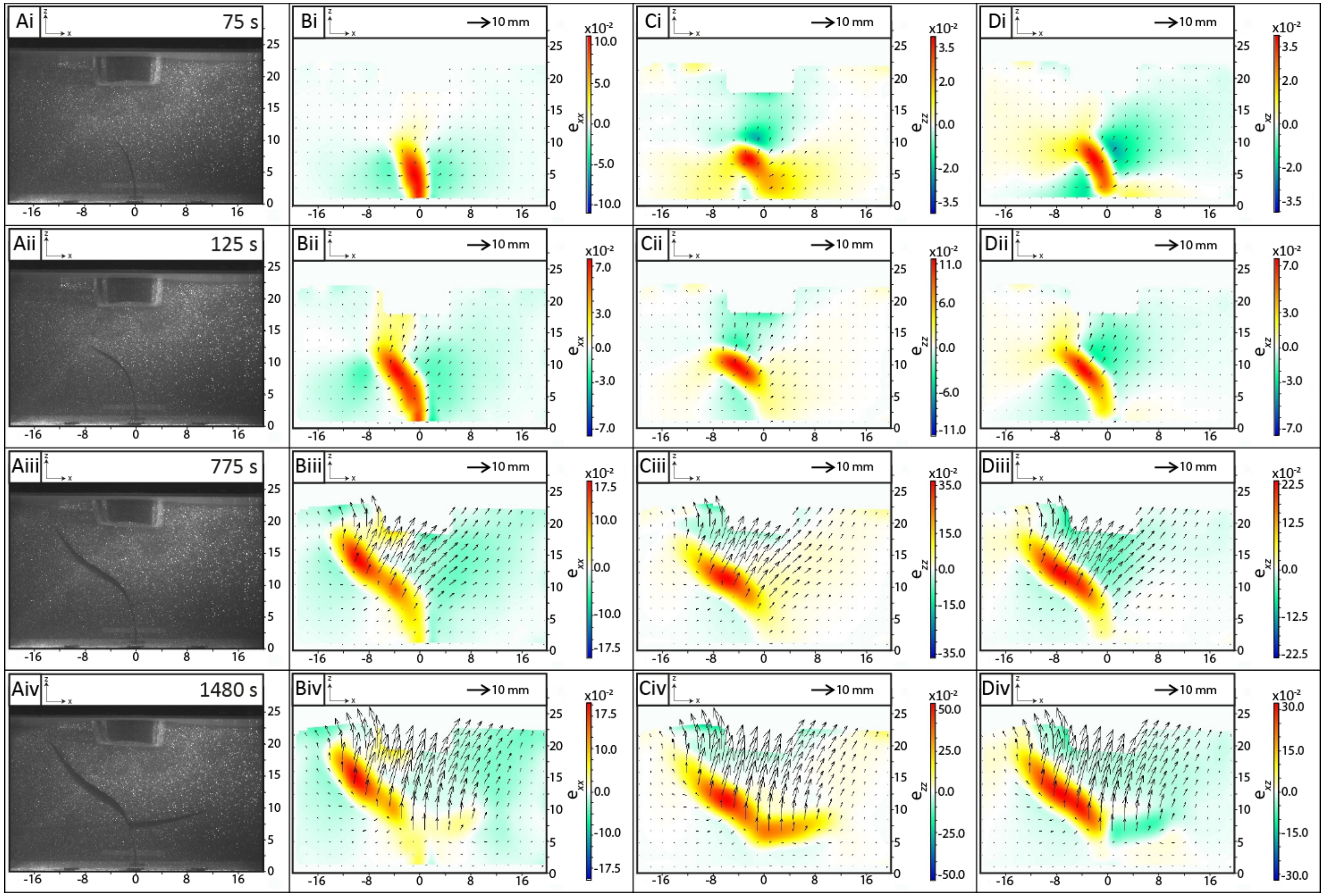

Figure 6: Cone sheet development in the presence of a large caldera, viewed in the x-z plane, with sub-surface total strain (color maps) and displacement (vector arrows) calculated using DIC (Experiment AG-17, see Table 1). Four stages of cone sheet development are shown: i) Stage I: initial sub-vertical dike (75 s), ii) Stage II: inclined sheet (125 s), iii) Stage III: arrest and increased opening of the inclined sheet (775 s), and iv) Stage IV: cone sheet geometry completion with no eruption (1480 s). A) Dewarped experimental images, B) horizontal total normal strain e_{xx}, C) vertical normal strain e_{zz}, and D) shear strain component e_{xz}. The red color represents extensional deformation in the normal components and anticlockwise rotational deformation in the shear component. See also Supplementary Video Figure S3.

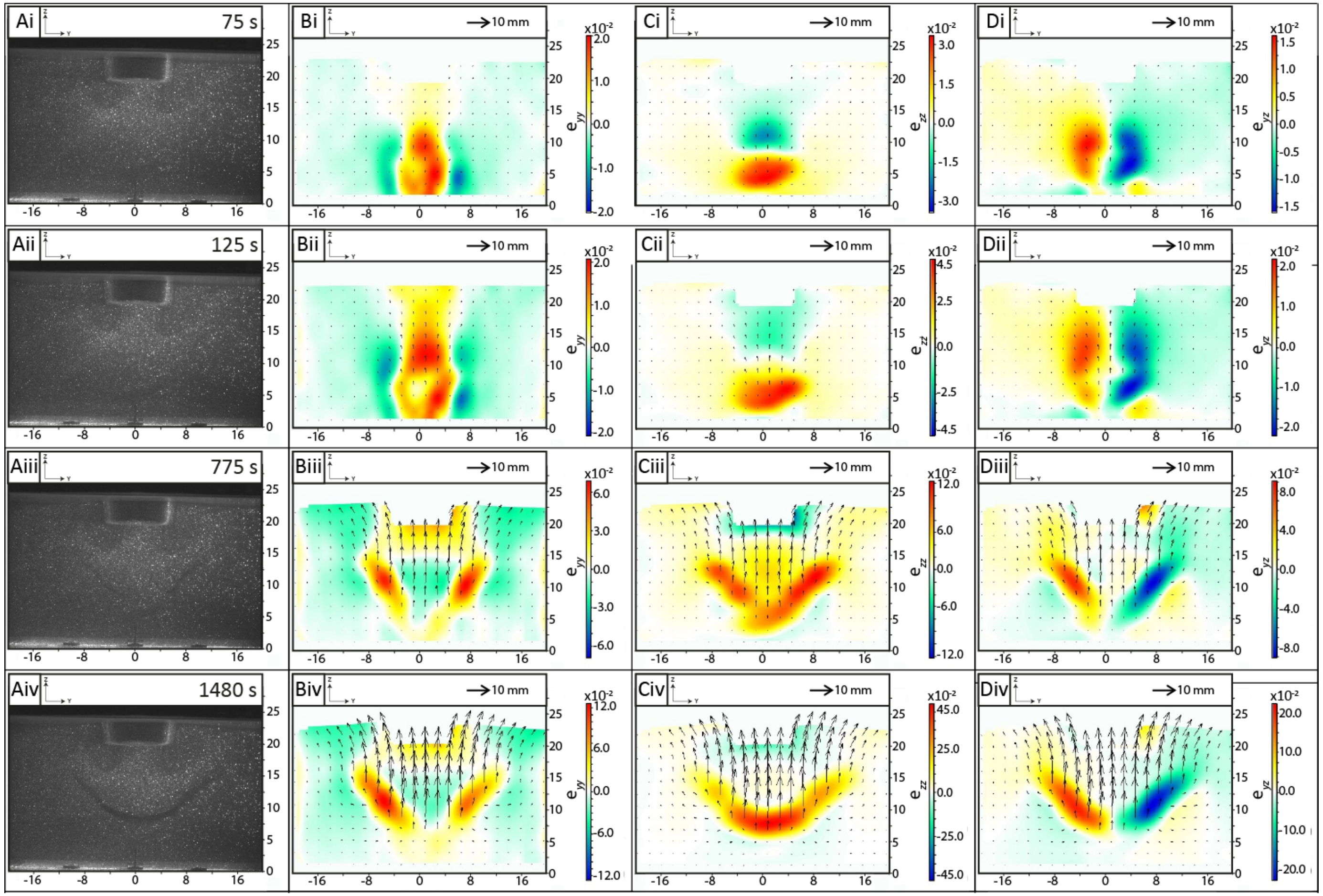

Figure 7: Cone sheet development in the presence of a large caldera, viewed in the y-z plane, with sub-surface total strain (color maps) and displacement (vector arrows) calculated using DIC (Experiment AG-19, see Table 1). Four stages of cone sheet development are shown: i) Stage I: initial sub-vertical dike (75 s), ii) Stage II: inclined sheet (125 s), iii) Stage III: arrest and increased opening of the inclined sheet (775 s), and iv) Stage IV: cone sheet geometry completion with no eruption (1480 s). A) Dewarped experimental images, B) horizontal normal strain e_{yy}, C) vertical normal strain e_{zz}, and D) shear strain component e_{yz}. The red color represents extensional deformation in the normal components and anticlockwise rotational deformation in the shear component. See also Supplementary Video Figure S4.

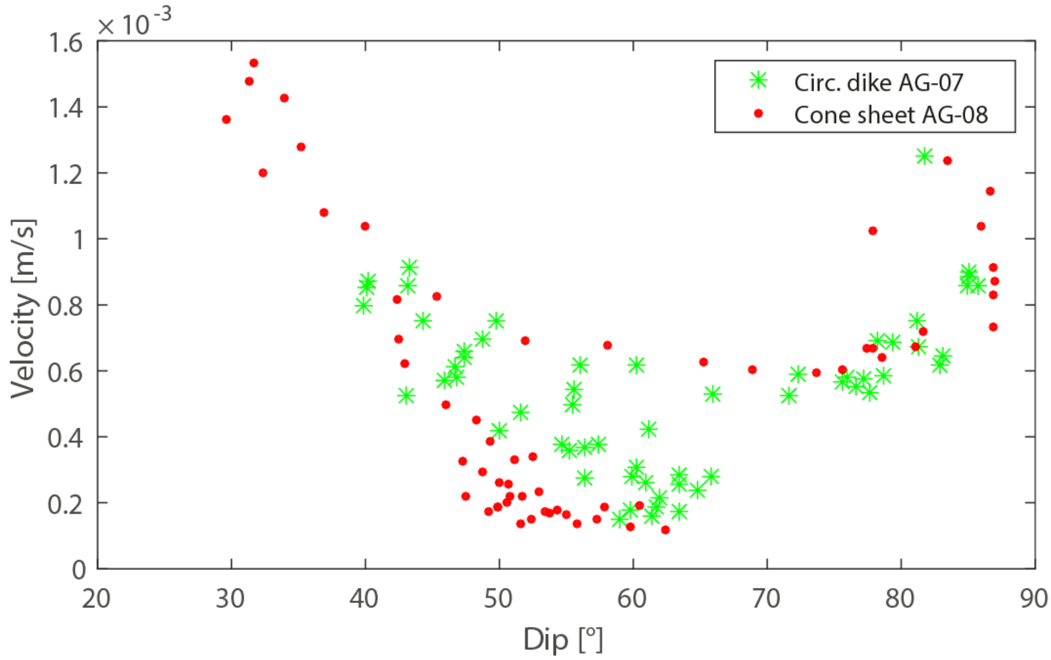

Figure 8: The local dip angle relative to vertical ascent velocity for circumferential dike (AG-07) and cone sheet development (AG-08). See Table 1 for experimental conditions.

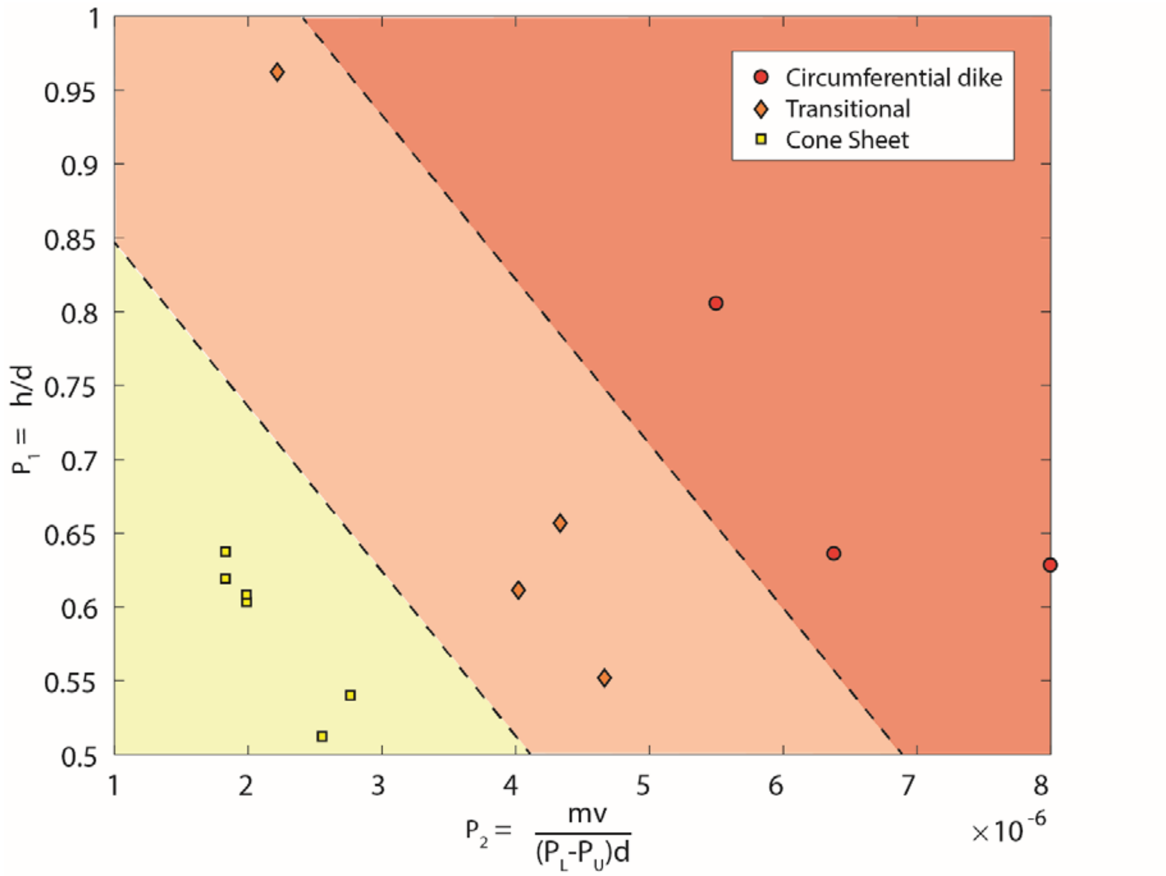

Figure 9: Dimensionless phase diagram presenting the range of intrusion geometries formed in the experiments: circumferential dikes (red circles), Transitional geometries (orange diamonds) and cone sheets (yellow squares). The dimensionless parameters represent the model conditions $\Pi_1 = h/d$ and $\Pi_2 = \mu v/(P_L - P_U)d$. The cone sheets and circumferential dikes plot in distinct fields with transitional geometries formed in the intermediate zone.

	Parameter (units) or Equation	Nature (range)	Nature (preferred value)	Experiments (range)	Experiments (preferred value)	Scaling ratio
Medium and fluid properties						
Host medium density[1]	ρ_r (kg m^{-3})	2300 - 3000	2700	994 – 1002	1002	0.37
Fluid density[2]	ρ_f (kg m^{-3})	2000 - 2800	2680	990 – 996	996	0.37
Fluid viscosity[10]	μ (Pa s)	0.1 – 1E+23	100	8.9E-4	8.9E-4	8.9E-6
Density difference[3]	$\Delta\rho = \rho_r - \rho_f$	1 - 300	20	4 - 6	6	0.3
Poisson's ratio[4]	ν	0.1 – 0.35	0.25	0.495-0.5	0.499	2
Fracture toughness[5]	K_c (Pa $m^{1/2}$)	3E+8 – 1E+9	1E+9	24 - 80	80	8E-8
Acceleration due to gravity	g (m s^{-2})	-	10	-	10	1
Geometry						
Geometric length	L (m)	-	1E+3	-	0.01	1E-5
Caldera diameter	C (m)	9E+3 – 12E+3	12E+3	0.09 – 0.12	0.12	1E-5
Caldera depth	D (m)	3E+3 – 4.5E+3	4E+3	0.03 – 0.045	0.04	1E-5
Depth of intrusion[11]	h (m)	3E+3 – 17E+3	13.5E+3	0.08 – 0.16	0.15	1.1E-5
Scaling expressions						
Lengths						
Buoyancy length[6]	$L_b=(K_c/(\pi^{1/2}\Delta\rho g))^{2/3}$	3.2E+3 – 6.6E+4	19965	0.83 – 1.22	0.83	4.1E-5
Stresses						
Elastic deformation[7]	$\sigma = Ee$	1E+6 - 4E+7	2E+7	4.5 - 75	60	3E-6
Lithostatic load	$P_L=\rho_r gh$	6.7E+7 – 5E+8	3.6E+8	779 - 1571	1473	4.1E-6
Unloading[8]	$P_U=\rho_r gD$	6.9E+7 – 1.3E+8	1.1E+8	298 – 451	401	3.7E-6
Young's Modulus[9]	E	1E+9 - 1E+10	1E+10	300 - 3000	3000	3E-7
Strain						
Thickness/width	e	1E-3 - 4E-3	2E-3	1.5E-2 - 2.5E-2	2E-2	10

Supplementary Table S1: Parameters and equations implemented to scale the experiments, including their ranges and the preferred values we have selected in nature and the experiments ([1] Carmichael and Klein, 2018; Di Giuseppe et al., 2009, [2] Murase and McBirney, 1973, [3,5] Kavanagh et al., 2013; Rivalta et al., 2015; [4] Gercek, 2007, [6,8,9] Kavanagh et al., 2013; Rivalta et al., 2015, [8] Merle, 2015, [10]Rivalta et al., 2015, [11]Kennedy et al., 2018).

Load	Mass [kg], m	Thickness [m]	Diameter [m], ψ
L1	0.05	0.012	0.025
L2	0.042	0.010	0.025

Supplementary Table S2: Properties of the two cylindrical brass loads used to measure the Young's modulus.

Video Figure S1: Experimental circumferential dike formation and propagation (all videos 30 frames per second): a)-b) Experiment AG-07 viewed with a) polarized light (x-z plane), and b) artificial light (y-z plane), c)-f) Experiment AG-13 (x-z plane) viewed with laser light (c), and total strain (color maps: horizontal E_{xx} (d), vertical E_{zz} (e), and shear E_{xz} (f) components) and displacement (vector arrows) calculated using digital image correlation. The red color represents extensional deformation in the normal components and anticlockwise rotational in the shear component.

Video Figure S2: Experimental cone sheet formation and propagation (experiment AG-08, 30 frames per second): a) viewed with polarized light (x-z plane), and b) viewed with artificial light (y-z plane).

Video Figure S3: Experimental cone sheet formation and propagation (experiment AG-17, x-z plane, all videos 30 frames per second): a) Viewed with laser light, b)-d) total strain (color maps: horizontal E_{xx} (b), vertical E_{zz} (c), and shear E_{xz} (d) components) and displacement (vector arrows) calculated using digital image correlation. The red color represents extensional deformation in the normal components and anticlockwise rotational in the shear component.

Video Figure S4: Experimental cone sheet formation and propagation (experiment AG-19, y-z plane, all videos 30 frames per second): a) Viewed with laser light, b)-d) total strain (horizontal E_{yy} (b), vertical E_{zz} (c), and shear E_{yz} (d) components) and displacement (vector arrows) calculated using digital image correlation. The red color represents extensional deformation in the normal components and anticlockwise rotational in the shear component.

References:

Anderson, E.M., 1936. The dynamics of the formation of cone-sheets, ring dykes, and caldron-subsidence. R. Soc. Edinburgh Proc. 56, 128–163. doi:10.1017/S0370164600014954

Bagnardi, M., Amelung, F., Poland, M.P., 2013. A new model for the growth of basaltic shields based on deformation of Fernandina volcano, Galápagos Islands. Earth Planet. Sci. Lett. 377–378, 358–366. doi:10.1016/j.epsl.2013.07.016

Blundy, J., Mavrogenes, J., Tattitch, B., Sparks, S., Gilmer, A., 2015. Generation of porphyry copper deposits by gas-brine reaction in volcanic arcs. Nat. Geosci. 8, 235–240. doi:10.1038/ngeo2351

Brown, D., 2012. Tracker Video Analysis and Modeling Tool for Physics Education [WWW Document]. URL http://physlets.org/tracker/ (accessed 9.21.17).

Brown, D.J., Bell, B.R., 2006. Intrusion-induced uplift and mass wasting of the Palaeogene volcanic landscape of Ardnamurchan, NW Scotland. J. Geol. Soc. London. 163, 29–36. doi:10.1144/0016-764905-016

Browning, J., Gudmundsson, A., 2015. Caldera faults capture and deflect inclined sheets: an alternative mechanism of ring dike formation. Bull. Volcanol. 77, 4. doi:10.1007/s00445-014-0889-4

Burchardt, S., Tanner, D.C., Troll, V.R., Krumbholz, M., Gustafsson, L.E., 2011. Three-dimensional geometry of concentric intrusive sheet swarms in the Geitafell and the Dyrfjöll volcanoes, eastern Iceland. Geochemistry, Geophys. Geosystems 12, 1–21. doi:10.1029/2011GC003527

Burchardt, S., Troll, V.R., Mathieu, L., Emeleus, H.C., Donaldson, C.H., 2013. Ardnamurchan 3D cone-sheet architecture explained by a single elongate magma chamber. Sci. Rep. 3, 1–7. doi:10.1038/srep02891

Burchardt, S., Walter, T.R., Tuffen, H., 2018. Growth of a Volcanic Edifice Through Plumbing System Processes—Volcanic Rift Zones, Magmatic Sheet-Intrusion Swarms and Long-Lived Conduits. Volcan. Igneous Plumb. Syst. 89–112. doi:10.1016/B978-0-12-809749-6.00004-2

Carmichael, R.S., Klein, C., 2018. Rock [WWW Document]. Encycl. Br. inc. URL https://www.britannica.com/science/rock-geology (accessed 7.26.18).

Chadwick, W.W., Jónsson, S., Geist, D.J., Poland, M., Johnson, D.J., Batt, S., Harpp, K.S., Ruiz, A., 2011. The May 2005 eruption of Fernandina volcano, Galápagos: The first circumferential dike intrusion observed by GPS and InSAR. Bull. Volcanol. 73, 679–697. doi:10.1007/s00445-010-0433-0

Cole, J.W., Milner, D.M., Spinks, K.D., 2005. Calderas and caldera structures: A review. Earth-Science Rev. 69, 1–26. doi:10.1016/j.earscirev.2004.06.004

Corbi, F., Rivalta, E., Pinel, V., Maccaferri, F., Acocella, V., 2016. Understanding the link between circumferential dikes and eruptive fissures around calderas based on numerical and analog models. Geophys. Res. Lett. 43, 6212–6219. doi:10.1002/2016GL068721

Corbi, F., Rivalta, E., Pinel, V., Maccaferri, F., Bagnardi, M., Acocella, V., 2015. How caldera collapse shapes the shallow emplacement and transfer of magma in active volcanoes. Earth Planet. Sci. Lett. 431, 287–293. doi:10.1016/j.epsl.2015.09.028

Crisp, J., 1952. The Use of Gelatin Models in Structural Analysis. Proceeding IB Inst. Mech. Eng. 12, 580–604.

Di Giuseppe, E., Funiciello, F., Corbi, F., Ranalli, G., Mojoli, G., 2009. Gelatins as rock analogs: A systematic study of their rheological and physical properties. Tectonophysics 473, 391–403. doi:10.1016/j.tecto.2009.03.012

Di Vito, M.A., Acocella, V., Aiello, G., Barra, D., Battaglia, M., Carandente, A., Del Gaudio, C., De Vita, S., Ricciardi, G.P., Ricco, C., Scandone, R., Terrasi, F., 2016. Magma transfer at Campi Flegrei caldera (Italy) before the 1538 AD eruption. Sci. Rep. 6, 32245. doi:10.1038/srep32245

Fleet, D., Weiss, Y., 2006. Optical Flow Estimation, in: Paragios, N., and Chen, Y., and Faugeras, O. (Eds.), Handbook of Mathematical Models in Computer Vision. Springer US, Boston, MA, pp. 239–257. doi:10.1109/TIP.2009.2032341

Galland, O., Bertelsen, H.S., Eide, C.H., Guldstrand, F., Haug, Ø.T., Leanza, H.A., Mair, K., Palma, O., Planke, S., Rabbel, O., Rogers, B., Schmiedel, T., Souche, A., Spacapan, J.B., 2018. Storage and Transport of Magma in the Layered Crust—Formation of Sills and Related Flat-Lying Intrusions, in: Volcanic and Igneous Plumbing Systems. pp. 113–138.

Galland, O., Burchardt, S., Hallot, E., Mourgues, R., Bulois, C., 2014. Dynamics of dikes versus cone sheets in volcanic systems. J. Geophys. Res. Solid Earth 6178–6192. doi:10.1002/2014JB011059.Received

Gercek, H., 2007. Poisson's ratio values for rocks. Int. J. Rock Mech. Min. Sci. doi:10.1016/j.ijrmms.2006.04.011

Geshi, N., 2005. Structural development of dike swarms controlled by the change of magma supply rate: The cone sheets and parallel dike swarms of the Miocene Otoge igneous complex, Central Japan. J. Volcanol. Geotherm. Res. 141, 267–281. doi:10.1016/j.jvolgeores.2004.11.002

Gudmundsson, A., 2006. How local stresses control magma-chamber ruptures, dyke injections, and eruptions in composite volcanoes. Earth-Science Rev. 79, 1–31. doi:10.1016/j.earscirev.2006.06.006

Guldstrand, F., Burchardt, S., Hallot, E., Galland, O., 2017. Dynamics of Surface Deformation Induced by Dikes and Cone Sheets in a Cohesive Coulomb Brittle Crust. J. Geophys. Res. Solid Earth 122, 8511–8524. doi:10.1002/2017JB014346

Jellinek, A.M., DePaolo, D.J., 2003. A model for the origin of large silicic magma chambers: Precursors of caldera-forming eruptions. Bull. Volcanol. 65, 363–381. doi:10.1007/s00445-003-0277-y

Johnson, S.E., Paterson, S.R., Tate, M.C., 1999. Structure and emplacement history of a multiple-center, cone-sheet bearing ring complex: The Zarza Intrusive Complex, Baja California, Mexico. Geol. Soc. Am. Bull. 111, 607–619.

Kavanagh, J.L., 2018. Mechanisms of Magma Transport in the Upper Crust—Dyking. Volcan. Igneous Plumb. Syst. 55–88. doi:10.1016/B978-0-12-809749-6.00003-0

Kavanagh, J.L., Boutelier, D., Cruden, A.R., 2015. The mechanics of sill inception, propagation and growth: Experimental evidence for rapid reduction in magmatic overpressure. Earth Planet. Sci. Lett. 421, 117–128. doi:10.1016/j.epsl.2015.03.038

Kavanagh, J.L., Burns, A.J., Hilmi Hazim, S., Wood, E.P., Martin, S.A., Hignett, S., Dennis, D.J.C., 2018. Challenging dyke ascent models using novel laboratory experiments:

Implications for reinterpreting evidence of magma ascent and volcanism. J. Volcanol. Geotherm. Res. 354, 87–101. doi:10.1016/j.jvolgeores.2018.01.002

Kavanagh, J.L., Engwell, S.L., Martin, S.A., 2018. A review of laboratory and numerical modelling in volcanology. Solid Earth 9, 531–571. doi:10.5194/se-9-531-2018

Kavanagh, J.L., Menand, T., Daniels, K.A., 2013. Gelatine as a crustal analogue: Determining elastic properties for modelling magmatic intrusions. Tectonophysics 582, 101–111. doi:10.1016/j.tecto.2012.09.032

Kavanagh, J.L., Menand, T., Sparks, R.S.J., 2006. An experimental investigation of sill formation and propagation in layered elastic media. Earth Planet. Sci. Lett. 245, 799–813. doi:10.1016/j.epsl.2006.03.025

Kennedy, B.M., Holohan, E.P., Stix, J., Gravley, D.M., Davidson, J.R.J., Cole, J.W., 2018. Magma plumbing beneath collapse caldera volcanic systems. Earth-Science Rev. 177, 404–424. doi:10.1016/j.earscirev.2017.12.002

Kervyn, M., Ernst, G.G.J., Van Wyk De Vries, B., Mathieu, L., Jacobs, P., 2009. Volcano load control on dyke propagation and vent distribution: Insights from analogue modeling. J. Geophys. Res. 114, 26. doi:10.1029/2008JB005653

Le Bas, M.J., 1987. Nephelinites and carbonatites. Geol. Soc. London, Spec. Publ. 30, 53–83. doi:10.1144/GSL.SP.1987.030.01.05

Maccaferri, F., Bonafede, M., Rivalta, E., 2011. A quantitative study of the mechanisms governing dike propagation, dike arrest and sill formation. J. Volcanol. Geotherm. Res. 208, 39–50. doi:10.1016/j.jvolgeores.2011.09.001

Magee, C., Stevenson, C., O'Driscoll, B., Schofield, N., McDermott, K., 2012. An alternative emplacement model for the classic Ardnamurchan cone sheet swarm, NW Scotland, involving lateral magma supply via regional dykes. J. Struct. Geol. 43, 73–91. doi:10.1016/j.jsg.2012.08.004

Mathieu, L., Burchardt, S., Troll, V.R., Krumbholz, M., Delcamp, A., 2015. Geological constraints on the dynamic emplacement of cone-sheets - The Ardnamurchan cone-sheet swarm, NW Scotland. J. Struct. Geol. 80, 133–141. doi:10.1016/j.jsg.2015.08.012

Mathieu, L., van Wyk de Vries, B., Holohan, E.P., Troll, V.R., 2008. Dykes, cups, saucers and sills: Analogue experiments on magma intrusion into brittle rocks. Earth Planet. Sci. Lett. 271, 1–13. doi:10.1016/J.EPSL.2008.02.020

McLeod, P., Tait, S., 1999. The growth of dykes from magma chambers. J. Volcanol. Geotherm. Res. 92, 231–245. doi:10.1016/S0377-0273(99)00053-0

Merle, O., 2015. The scaling of experiments on volcanic systems. Front. Earth Sci. 3, 1–15. doi:10.3389/feart.2015.00026

Murase, T., McBirney, A.R., 1973. Properties of some common igneous rocks and their melt at high temperatures. Geol. Soc. Am. Bull. 84, 3563–3592. doi:10.1130/0016-7606(1973)84%3C3563:POSCIR%3E2.0.CO;2

Pallister, J., Hoblitt, R., Meeker, G., 1996. Magma mixing at Mount Pinatubo: petrographic and chemical evidence from the 1991 deposits. Fire Mud Eruptions Lahars Mt. Pinatubo , Philipp. 1–27.

Pollard, D.D., Segall, P., Delaney, P.T., 1982. Formation and interpretation of dilatant echelon cracks. Geol. Soc. Am. Bull. 93, 1291–1303. doi:10.1130/0016-

7606(1982)93<1291:FAIODE>2.0.CO

Prejean, S., Stork, A., Ellsworth, W., Hill, D., Julian, B., 2003. High precision earthquake locations reveal seismogenic structure beneath Mammoth Mountain, California. Geophys. Res. Lett. 30. doi:10.1029/2003GL018334

Richey, J., Thomas, H., 1930. The Geology of Ardnamurchan, North-west Mull and Coll: Memoir for Geological Sheet 51, Part 52 (Scotland). HM Stationery Office.

Rivalta, E., Taisne, B., Bunger, A.P., Katz, R.F., 2015. A review of mechanical models of dike propagation: Schools of thought, results and future directions. Tectonophysics 638, 1–42. doi:10.1016/j.tecto.2014.10.003

Schirnick, C., Van Den Bogaard, P., Schmincke, H.U., 1999. Cone sheet formation and intrusive growth of an oceanic island-the Miocene Tejeda complex on Gran Canaria (Canary Islands). Geology 27, 207–210. doi:10.1130/0091-7613(1999)027<0207:CSFAIG>2.3.CO;2

Sutton, M., Wolters, W., Peters, W., Ranson, W., McNeill, S., 1983. Determination of displacements using an improved digital correlation method. Image Vis. Comput. 1, 133–139. doi:10.1016/0262-8856(83)90064-1

Taisne, B., Tait, S., 2009. Eruption versus intrusion? arrest of propagation of constant volume, buoyant, liquid-filled cracks in an elastic, brittle host. J. Geophys. Res. Solid Earth 114, B06202. doi:10.1029/2009JB006297

Takada, A., 1990. Experimental study on propagation of liquid-filled crack in gelatin: Shape and velocity in hydrostatic stress condition. J. Geophys. Res. 95, 8471. doi:10.1029/JB095iB06p08471

Troll, V.R., Emeleus, C.H., Donaldson, C.H., 2000. Caldera formation in the Rum Central Igneous Complex, Scotland. Bull. Volcanol. 62, 301–317. doi:10.1007/s004450000099

USGS, H.V.O., 2018. Preliminary Analysis of the ongoing Lower East Rift Zone (LERZ) eruption of Kīlauea Volcano : Fissure 8 Prognosis and Ongoing Hazards.

Watanabe, T., Masuyama, T., Nagaoka, K., Tahara, T., 2002. Analog experiments on magma-filled cracks : Competition between external stresses and internal pressure. Earth Planets Sp. 54, 1247–1261. doi:10.1186/BF03352453